Bulletin of the Seismological Society of America, Vol. 97, No. 6, pp. 2053–2065, December 2007, doi: 10.1785/0120070031

Geometric Spreading of P_n and S_n in a Spherical Earth Model

by Xiaoning Yang, Thorne Lay, Xiao-Bi Xie, and Michael S. Thorne

Abstract Geometric spreading of P_n and S_n waves in a spherical Earth model is different than that of classical headwaves and is frequency dependent. The behavior cannot be fully represented by a frequency-independent power-law model, as is commonly assumed. The lack of an accurate representation of P_n and S_n geometric spreading in a spherical Earth model impedes our ability to characterize Earth properties including anelasticity. We conduct numerical simulations to quantify P_n and S_n geometric spreading in a spherical Earth model with constant mantle-lid velocities. Based on our simulation results, we present new empirical P_n and S_n geometric-spreading models in the form $G(r, f) = [10^{n_3(f)}/r_0](r_0/r)^{n_1(f)\log(r_0/r)+n_2(f)}$ and $n_i(f) = n_{i1}[\log(f/f_0)]^2 + n_{i2}\log(f/f_0) + n_{i3}$, where $i = 1$, 2, or 3; r is epicentral distance; f is frequency; $r_0 = 1$ km; and $f_0 = 1$ Hz. We derive values of coefficients n_{ij} by fitting the model to computed P_n and S_n amplitudes for a spherical Earth model having a 40-km-thick crust, generic values of P and S velocities, and a constant-velocity uppermost mantle. We apply the new spreading model to observed data in Eurasia to estimate average P_n attenuation, obtaining more reasonable results compared to using a standard power-law model. Our new P_n and S_n geometric-spreading models provide generally applicable reference behavior for spherical Earth models with constant uppermost-mantle velocities.

Introduction

Seismic phases P_n and S_n are refracted waves that traverse the uppermost mantle and are typically the first P and S arrivals at distances from ~200 to ~1500 km. These phases are commonly characterized as being conical headwaves based on considerations of wave interactions with planar constant-velocity layered structures. However, the propagation of P_n and S_n in the actual spherical Earth is much more complex. In addition to the effects on P_n and S_n propagation of uppermost-mantle velocity complexities such as mantle-lid radial velocity gradients, lateral velocity heterogeneities, and depth variation of the Moho discontinuity, the curvature of both the Moho and the Earth's surface (the sphericity) alters P_n and S_n amplitudes profoundly from that of a headwave. Textbook treatments of the propagation of conical headwaves in plane crustal-layer-over-half-space models (e.g., Lay and Wallace, 1995; Aki and Richards, 2002) hold for a spherical Earth model only in the unlikely situation of a precisely critical negative velocity gradient below the Moho. Lesser negative velocity gradients, constant velocities, or positive velocity gradients in the mantle will all produce complex frequency-dependent behavior of P_n and S_n that is not the same as that of a conical headwave. At relatively short epicentral distances (less than a few hundred kilometers), the sphericity effects are negligible. But as epicentral distance increases, P_n and S_n behavior is strongly influenced by the sphericity, and one cannot ignore the need for formal mapping between plane-layered structures and spherical velocity structures. The effects of the sphericity must be accounted for when interpreting regional-phase seismic magnitudes, source-type discriminants using P_n and S_n, and frequency-dependent measures such as the attenuation of P_n and S_n. In this study, we quantify the sphericity effects on P_n and S_n geometric spreading through detailed numerical modeling.

The behavior of P_n and S_n in a spherical Earth model has been studied both theoretically and numerically since the 1960s. Buldyrev and Lanin (1965) and Hill (1973) investigated the propagation of S_n and P_n in and around an elastic spherical body by solving the wave equation using asymptotic methods. Červený and Ravindra (1971) used the ray method to characterize the phenomenon of P_n traveling in a plane-layered medium with a constant-velocity gradient in the mantle, which can be related to models with spherical boundaries through the Earth flattening transformation (EFT) (e.g., Chapman, 1973; Müller, 1977). Sereno and Given (1990) conducted numerical simulations of P_n waves in a plane-layered Earth model generated from a spherically symmetric Earth model with the EFT. The conclusions from these studies using different approaches are that (1) the geometric spreading of P_n and S_n in a spherical Earth model differs significantly from that of conical headwaves for plane-layered structures; (2) the spreading cannot be accurately represented for all ranges by a simple power-law model; and (3) the spreading is frequency dependent, which is not the case for classic headwaves.

In spite of these conclusions, seismologists commonly use a frequency-independent power-law model to approximate P_n geometric spreading in the real Earth when analyzing observed data (e.g., Sereno *et al.*, 1988; Zhu *et al.*, 1991; Taylor *et al.*, 2002). Occasionally, researchers combine P_n geometric spreading and attenuation into a single distance-decay term in order to avoid the difficulty of isolating P_n geometric-spreading effects (e.g., Chun *et al.*, 1989; Tinker and Wallace, 1997). Because of the apparent incompatibility between the behavior of P_n in the real Earth and its power-law geometric-spreading representation, Taylor *et al.* (2002) postulated that the use of a frequency-independent power-law spreading model might be the reason for difficulties encountered in fitting the P_n spectra in their study. The common practice of representing P_n geometric spreading in the real Earth with a frequency-independent power-law model may simply be a choice of convenience due to the unavailability of a more accurate, easy-to-use, frequency-dependent P_n geometric-spreading model, even for a simple reference velocity structure. Although there exist theoretical solutions of waves propagating in an elastic body with spherical symmetry (Buldyrev and Lanin, 1965; Hill, 1973), they only describe high-frequency asymptotic wave behavior. These solutions are also too complex to be of general use in practical applications.

Building upon the insight provided by the P_n modeling of Sereno and Given (1990), we perform more detailed and rigorous numerical simulations in this study to establish appropriate P_n and S_n geometric-spreading relationships for the important class of continental 1D spherical Earth models with constant seismic velocities in the uppermost mantle. Prescribing a constant uppermost-mantle velocity is a common default given that detailed and reliable velocity structure and gradients in the mantle lid are either not available or not general enough to represent many parts of the uppermost mantle beneath continents. Based on our modeling results, we first propose a quantitative, frequency-dependent P_n geometric-spreading model. We then explore the implications of this new model on attenuation estimation using observed P_n amplitude data. We also investigate the variation of model parameters, due to variations of crustal thickness, source depth, and crust/mantle velocity contrast, and the resulting variation of attenuation estimates. Finally, we model S_n propagation under the same configuration and propose a similar geometric-spreading model for S_n. Even though our spreading models cannot account for all the complexities of P_n and S_n propagation in the real Earth, they serve as better first-order approximations of P_n and S_n geometric spreading in a spherical Earth than the standard power-law model.

Methodology

We conduct most of our simulations using the reflectivity method (Kennett, 1983; Randall, 1994). Results from reflectivity calculations are compared with results calculated with a 2D finite-difference code (Xie and Lay, 1994) and a 2.5D axisymmetric spherical finite-difference code, SHaxi (Igel and Weber, 1995) to confirm that the EFT and layer discretization required by the reflectivity method do not produce numerical artifacts.

The reflectivity method generates complete synthetic seismograms within a specified slowness range for 1D plane-layered velocity models. In order to use the reflectivity method for a spherically symmetric Earth model, we apply the EFT to transform the spherical Earth model to a plane Earth model. Transformations of velocity v and depth z are (Chapman, 1973; Müller, 1977)

$$v_f = \frac{R}{R - z_r} v_r \quad \text{and} \quad z_f = R \ln\left(\frac{R}{R - z_r}\right), \tag{1}$$

where R is the radius of the Earth. Subscript r designates values in the spherical (radially symmetric) model, and subscript f designates values in the plane (flat) model. The density ρ transformation is

$$\rho_f = \left(\frac{R}{R - z_r}\right)^m \rho_r, \tag{2}$$

which is not unique because m can take any value between -5 and 1. For regional body waves, the choice of m is not critical (Müller, 1977). We choose $m = -1$ for P/SV simulations (Müller, 1977) and $m = -5$ for SH simulations (Chapman, 1973). We experimented with different values of m and the results were basically unchanged. Finally the transformation of amplitudes calculated from plane-model simulations back to corresponding amplitudes in the spherical model is

$$A_r = \left(\frac{\Delta}{\sin \Delta}\right)^{1/2} \left(\frac{R}{R - Z_r}\right)^{(m+5)/2} A_f, \tag{3}$$

where Z_r is the depth of the source in the spherical model and Δ is epicentral distance in radians.

We approximate the velocity gradient resulting from the EFT (equations 1 and 2) with homogeneous layers in the plane Earth model, as is required by the reflectivity method. The thickness of these layers affects the accuracy of the approximation, with thinner layers yielding more accurate results. We set the thickness of these layers to be about 0.4 of the minimum wavelength of the waves to be modeled, which appears to be more than adequate (Chapman and Orcutt, 1985). Further reducing the ratio (e.g., from 0.4 to 0.2 of the minimum wavelength) does not alter the results appreciably. The total thickness of the gradient zone is set to be more than 100 km larger than the maximum penetration depth of the direct wave in a homogeneous spherical model recorded at the longest epicentral distance considered. This thickness guarantees that no P_n or S_n waves observed within the distance range of interest are affected by the lower boundary of the gradient zone. Below the gradient zone, the velocity is constant.

We use the same generic spherical Earth model considered by Sereno and Given (1990) as the reference model for our simulations and use the synthetics from the simulation to derive parameters of the P_n and S_n geometric-spreading models that we develop. The reference Earth model consists of a 40-km-thick outer layer, representative of an average continental crust, with a constant-velocity mantle underneath (Fig. 1). The model has no anelastic attenuation. The simplicity of this model allows us to isolate the effects of the sphericity on P_n and S_n geometric spreading. We use an isotropic point source for P_n simulations. The source for $S_n(SH)$ simulations is a vertical strike-slip source, and the source for $S_n(SV)$ simulations is a vertical dip-slip source. For all source types in our main calculations, a delta function is used as the source time function; source depth is 15 km, and source strength is 10^{15} N m. Three-component synthetic ground displacements are computed at 33 locations distributed log-evenly along a linear profile from 200 (1.8°) to 2500 km (22.5°). The Nyquist frequency of the seismograms is 20 Hz.

We cut P_n and S_n portions of the synthetic seismograms using fixed-velocity windows. The velocities that we use to define the widths of the P_n windows are7.6 and 8.2 km/sec, and those for S_n windows are 4.0 and 4.7 km/sec (Hartse, *et al.*, 1997). The windows are centered at the peaks of the phases. We also tested a fixed-window-width method, and the results remained essentially the same. We window P_n and $S_n(SV)$ from vertical-component seismograms and $S_n(SH)$ from transverse-component seismograms. After P_n and S_n seismograms are windowed, we taper the seismograms with small tapers (between 2% to 20% depending on the length of the signal relative to the window length) and Fourier transform the seismograms to obtain the amplitude spectra. We make spectral-amplitude measurements at 100 frequencies log-evenly distributed between 0.75 and 13 Hz. Amplitude at each frequency f_i is calculated by taking the average of the amplitudes between frequencies $f_i/\sqrt{2}$ and $\sqrt{2}f_i$ (Bowman and Kennett, 1991; Hartse *et al.*, 1997).

To accurately assess the geometric spreading of seismic phases, the propagation medium used for the simulation should have no attenuation. However, in order to avoid a computational singularity, the reflectivity method requires a nonzero amount of attenuation for the medium. We take an asymptotic approach similar to that used by Yang (2002) to derive P_n and S_n amplitudes for an elastic model without attenuation from amplitudes calculated for a group of anelastic models. We first make 20 calculations for models that have attenuation quality factor Q log-linearly increasing from 10,000 to 100,000. For each calculation, a single Q is used for both P and S waves and for all parts of the model. Amplitudes at each frequency and each epicentral distance from these calculations are then fit by a quadratic polynomial as a function of $1/Q$. The limit of the polynomial as Q approaches infinity is taken as the amplitude at that frequency and distance for the elastic model.

P_n Modeling Results

Figure 2 plots the vertical synthetic P_n seismograms from the reference-model simulation at selected epicentral distances. Q used in this simulation is 100,000. The seismograms are low-pass filtered below 10 Hz to suppress numerical noise near the Nyquist frequency. The figure reveals several interesting characteristics of P_n traveling in a

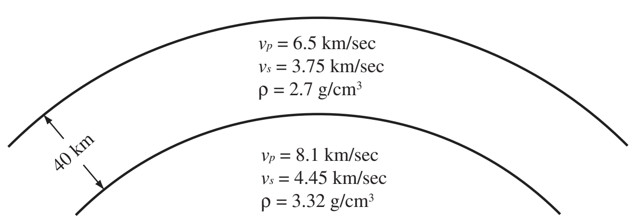

Figure 1. Reference Earth model used for P_n and S_n simulations and the development of new P_n and S_n geometric-spreading models. Quality factor Q is infinite throughout the model.

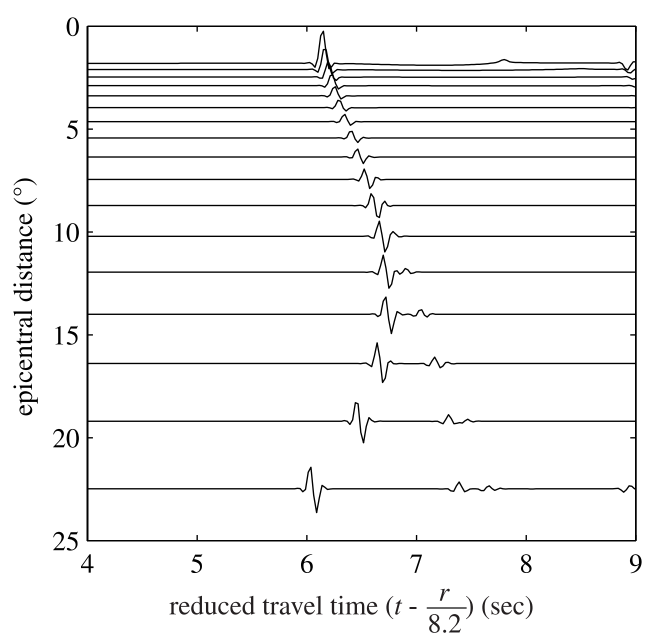

Figure 2. Synthetic P_n seismograms from reference-model calculations. The seismograms are filtered below 10 Hz. Travel time is reduced by 8.2 km/sec. Only every other trace calculated is plotted to enhance clarity. r is the epicentral distance in kilometers.

spherical Earth model with constant mantle velocities. Due to the sphericity, the apparent P_n velocity is not constant but varies with epicentral distance. As is predicted by theory (e.g., Červený and Ravindra, 1971), the pulse shape of P_n evolves from that of the impulse source at distances close to the critical distance (about 0.8° for the reference model and a 15-km-deep source) to the shape of a far-field body wave, which is the time derivative of the source pulse, at farther distances. The amplitude of the phase changes in a complex manner, first decreasing and then increasing, within this distance range. At about 10° to 12°, the first pulse separates from the rest of the P_n wave packet, and somewhere between 16° and 19°, a second pulse separates.

For high-frequency P_n at distances away from the critical distance, Červený and Ravindra (1971) offer a detailed description of the signal behavior from ray theory. Although Červený and Ravindra (1971) describe the phenomenon for a plane-layered Earth model with a positive and constant-velocity gradient in the mantle, their description and conclusions are applicable to the spherical Earth model situation as well because the spherical model can be mapped, through the EFT, into a plane-layered model with an approximately constant-velocity gradient in the uppermost mantle. Following Červený and Ravindra (1971), the P_n phase at distances between about 5° and 10° in Figure 2 can be thought of as the superposition of individual waves reflected n times ($n = 0$, 1, 2, …) from the underside of the Moho. The superposed wave is termed interference headwaves by Červený and Ravindra (1971) and is likened to the "whispering gallery" phenomenon by Menke and Richards (1980). As distance increases, individual components of the interference headwave start to separate from the wave packet due to their increasingly shorter path lengths compared with path lengths of the remaining waves in the wave packet. The first wave to separate is the wave that has no reflection at the Moho (the direct or diving wave). This is evidenced as the separation of the first pulse in Figure 2. The second separated pulse in the figure is the wave that is reflected once from the Moho. From ray theory, the epicentral distance at which the k-time reflected wave separates from the interference headwave packet is (Červený and Ravindra, 1971, equation 6.4)

$$r_k = (2H - d)\frac{v_c}{\sqrt{v_m^2 - v_c^2}} + \left[\frac{32 v_m^3 T(1+k)^2(1+\frac{1}{2}k)^2}{g^2(1+\frac{2}{3}k)}\right]^{1/3}, \tag{4}$$

where H is the crustal thickness; d is the source depth; v_c is the P-wave velocity of the crust; v_m is the P-wave velocity at the top of the mantle; T is the pulse width of the wave, and g is the velocity gradient (dv/dz) at the top of the mantle resulting from the EFT. From equation (4) and for the reference model, a wave with a pulse width of about 0.1 sec (10 Hz) that undergoes no reflection at the Moho will separate at about 9.8°, and the wave that has one reflection will separate at about 16.6°. These predictions are consistent with the synthetics in Figure 2.

Figure 3 shows the amplitude spectra of synthetic P_n at the same epicentral distances as those in Figure 2 from the $Q = 100,000$ computation. The figure illustrates the evolution of the P_n spectrum from being proportional to the source spectrum to being proportional to the time derivative of the source spectrum.

As was described in the last section, we use an asymptotic method to derive spectral amplitudes for an elastic model from amplitudes obtained using anelastic simulations. Figure 4 gives an illustration of the method. Plotted in the figure are P_n amplitudes at different frequencies measured from calculations using different quality factors. The amplitudes are computed at 22.5° epicentral distance and are normalized by the maximum amplitude in the figure. Quadratic polynomial fits of the amplitudes are plotted as solid lines. The polynomial fits are almost perfect, indicating that our approach is appropriate. Amplitudes at other distances are fit as well as those shown in Figure 4.

To visualize the P_n amplitude decay in a spherical Earth model, we plot 10-Hz P_n amplitudes for the reference model in Figure 5. We extend the epicentral-distance range to between 135 (1.2°) and 8000 km (71.9°) for this particular simulation in order to better depict the evolution of P_n waves. Amplitudes at distances beyond about 20° are measured from the direct wave that has been completely separated from the interference headwaves. The amplitudes are corrected for the free-surface effect (the Appendix), which is only important at teleseismic distances. Also plotted in the figure are the amplitude decay of a conical headwave in a plane one-layer-over-half-space model (Aki and Richards, 2002; equa-

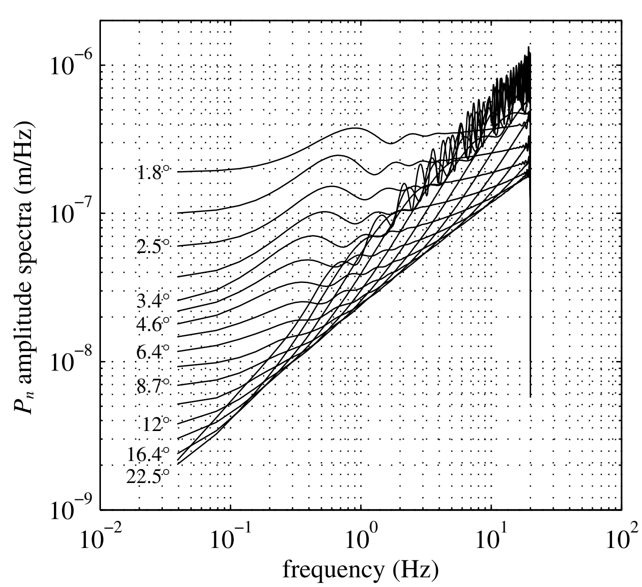

Figure 3. Amplitude spectra of P_n at the same distances as those in Figure 2. Some of the distances are marked on the left of the corresponding spectra.

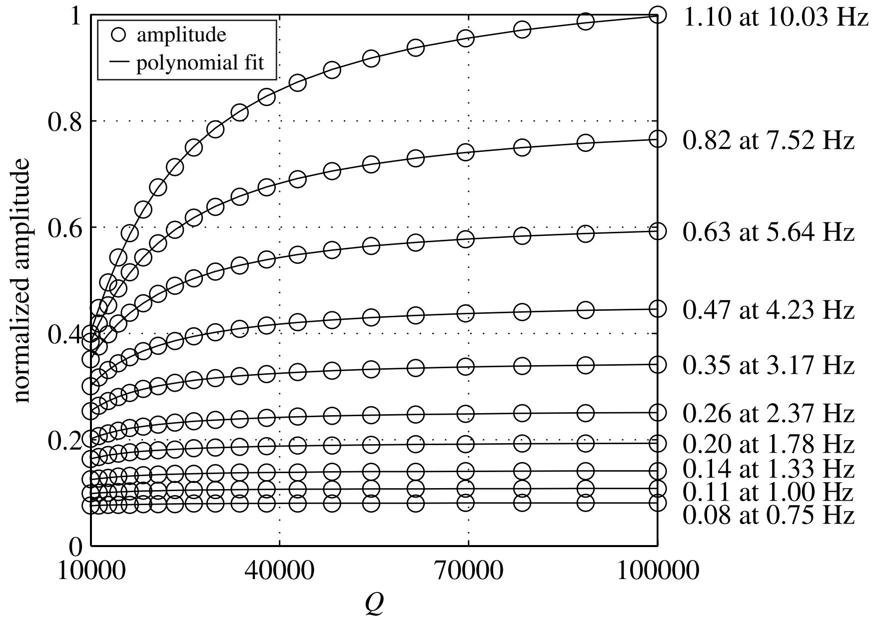

Figure 4. An illustration of how elastic results are obtained from anelastic calculations. Circles are amplitudes at 22.5° epicentral distance for different frequencies plotted against Q used in their calculations. The amplitudes are normalized by the maximum amplitude in the plot, which is the 10.03-Hz amplitude from the $Q = 100,000$ calculation. Solid lines are corresponding quadratic polynomial fits of the amplitudes. Numbers on the right are the limits of normalized amplitudes at corresponding frequencies as Q approaches infinity.

tion 6.26) and the amplitude decay of a infinite-frequency direct wave in a spherical Earth model from ray tracing. At distances close to the critical distance, P_n geometric spreading behaves like that of a conical headwave. As distance increases, P_n spreading starts to deviate from that of the headwave, and at about 5°, P_n amplitudes begin to increase. As was mentioned before, 10-Hz direct-wave energy would separate from the rest of the interference headwave at about 10°. It seems from the figure that this separation is manifested in a change in the smoothness of the P_n amplitude variation followed by a reduced rate of amplitude increase. In the range beyond the critical distance and before the direct-wave separation, P_n evolves from a wave similar to a conical headwave to the interference headwave, which is a superposition of multiple waves reflected from the Moho. As the epicentral distance approaches teleseismic distances, the direct-wave spreading approaches that of the infinite-frequency wave from ray tracing results, as is expected. The direct wave dominates the whole P_n wave packet at long distances. We do not see a significant difference between spectral amplitudes obtained by windowing the whole P_n wave packet and those obtained by windowing just the direct wave after its separation from the packet. This is consistent with theoretical predictions (Červený and Ravindra, 1971).

P_n geometric spreading in a spherical Earth model is not only different from that of a head wave, as is shown in Figure 5, but also is frequency dependent. Figure 6 shows the P_n amplitude-variation surface as a function of distance and frequency for the reference model. The strong frequency dependence of the amplitudes is apparent. Amplitudes at higher frequencies are affected more by the sphericity than are lower-frequency amplitudes. The separation distance of the direct wave from the interference headwaves becomes shorter as frequency becomes higher (equation 4).

A New P_n Geometric-Spreading Representation for a Spherical Earth Model

Figures 5 and 6 illustrate that a frequency-independent power-law model cannot accurately represent P_n geometric spreading in a spherical Earth model. Such a representation would plot as a straight line in Figure 5, which is clearly inappropriate for modeling P_n geometric spreading over a wide distance range. In addition, a power-law model with a constant exponent does not take into account the frequency dependence of P_n spreading shown in Figure 6. Based on the P_n amplitude-decay behavior shown in Figures 5 and 6, we propose a new empirical P_n geometric-spreading model that fits the synthetic data much better and that also results in more reasonable anelastic-attenuation estimates from observed data, as we will discuss in more detail in the next section.

The amplitude spectrum of P_n can be parameterized as

$$A(r, \theta, f) = K(f) M_0 R(\theta) G(r, f) \exp\left(-\frac{\pi f}{Q(f) v} r\right) S(f), \tag{5}$$

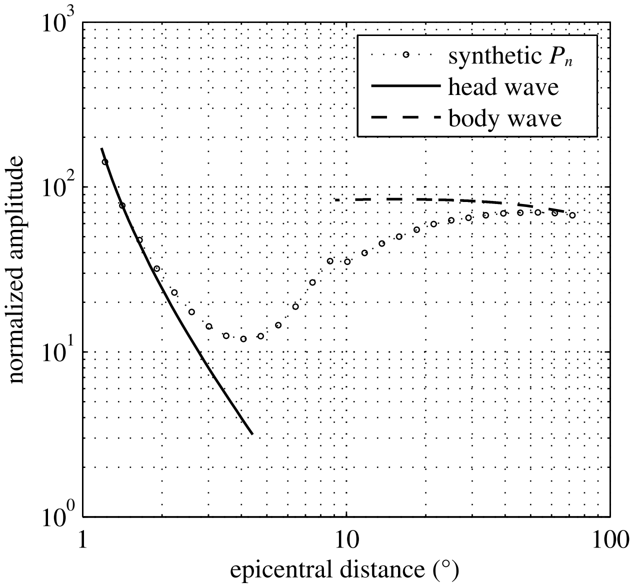

Figure 5. 10-Hz synthetic P_n amplitude decay in a spherical Earth model with constant mantle velocities. The solid line depicts the theoretical amplitude decay of a conical headwave in a plane one-layer-over-half-space Earth model. The dashed line is the amplitude decay of the infinite-frequency direct wave in a spherical homogeneous Earth model from ray-tracing calculations. Because we are interested in comparing only the decay of the amplitude curves, they are shifted in the vertical direction arbitrarily (normalized) so that they overlap.

with the new geometric-spreading model expressed as

$$G(r,f) = \frac{10^{n_3(f)}}{r_0}\left(\frac{r_0}{r}\right)^{n_1(f)\log(r_0/r)+n_2(f)} \qquad (r_0 = 1 \text{ km}) \tag{6}$$

and

$$n_i(f) = n_{i1}\left[\log\left(\frac{f}{f_0}\right)\right]^2 + n_{i2}\log\left(\frac{f}{f_0}\right) + n_{i3} \quad (i = 1,2,3; f_0 = 1 \text{ Hz}). \tag{7}$$

In equation (5), K is a frequency-dependent scaling factor; M_0 is the source moment; R is the source radiation pattern; Q is the P_n quality factor; v is the P_n velocity; S is the receiver site response; r is the epicentral distance; θ is the azimuth angle, and f is frequency. r_0 and f_0 are included in equations (6) and (7) in order for the new model to have the same dimension as standard power-law models (e.g., Street *et al.*, 1975; Sereno *et al.*, 1988). The main differences between the new geometric-spreading model (equations 6 and 7) and the standard frequency-independent power-law model are the addition of the first term in the exponent and the frequency dependence of parameters n_i. In the logarithm domain, the new model is a quadratic function of log-distance, whereas the power-law model is linear. The reason

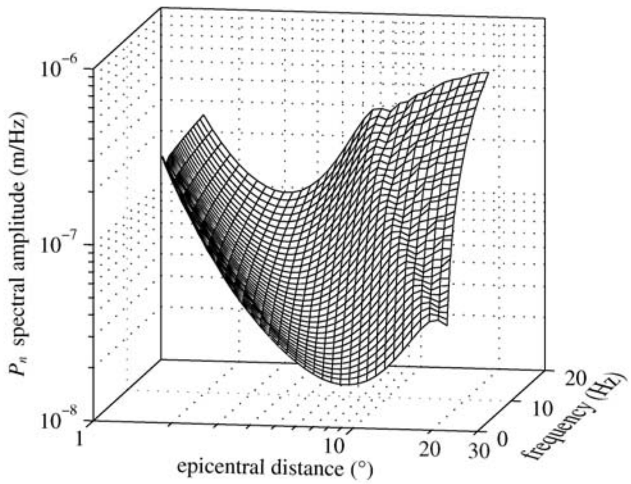

Figure 6. Synthetic P_n amplitudes as a function of epicentral distance and frequency.

for choosing a log-quadratic function is to keep the parameterization as simple as possible while providing a good fit to the synthetics. The adoption of a quadratic functional form for n_i (equation 7) is based on the behavior of n_i versus the frequency obtained by fitting equation (6) to synthetic P_n amplitudes at individual frequencies.

If we take the common logarithm of equation (6), substitute equation (7) into the result, and let r_0 and f_0 equal one, we obtain

$$\begin{aligned}\log[G(r,f)] = {} & n_{11}(\log f)^2(\log r)^2 + n_{12}\log f(\log r)^2 \\ & + n_{13}(\log r)^2 - n_{21}(\log f)^2\log r \\ & - n_{22}\log f\log r - n_{23}\log r + n_{31}(\log f)^2 \\ & + n_{32}\log f + n_{33},\end{aligned} \tag{8}$$

where r is in kilometers and f is in hertz. To derive coefficients n_{ij}, we fit equation (8) to synthetic P_n amplitudes shown in Figure 6 in a least-squares sense. P_n amplitudes are corrected for M_0 used in the simulation (10^{15} N m) and K before the fitting. Because the source that we use in the simulation has a flat spectrum, K is frequency independent. We use $K = (4\pi\rho v^3)^{-1}$ (Denny and Johnson, 1991), where ρ is the density and v is the P-wave velocity of the source region. Source radiation and site response are unity. We use P_n amplitudes at epicentral distances beyond 300 km (2.7°) and before the start of the direct-wave separation to fit the model. We use 300 km as the lower distance limit because reliable P_n observations are typically made at some distances beyond the P_g crossover distance (~200 km). The choice of 300 km is also to avoid possible long-period numeric-noise contamination at short distances, as is indicated in Figure 6. The upper distance limits are based on the observation that within these distances P_n is the result of the interference of all of its components including the direct wave. At larger distances, the direct wave separates from the rest of the wave packet, and the characteristics of P_n become different. The P_n amplitude decay within the defined distance range also has a smooth pattern and thus is easier to fit by a simple mathematical model. The upper distance limits vary from 7.3° to 17.3° for the frequency range between 13 and 0.75 Hz. Within the specified distance limits, the new spreading model is applicable. Because at about 15° P_n in the real Earth is overtaken by upper-mantle triplications resulting from reflections and refractions at 410- and 660-km discontinuities (e.g., Lay and Wallace, 1995) and is no longer the first arrival, P_n is usually used within the distance range where the new spreading model is valid for frequencies below about 2 Hz. For higher frequencies, the range of applicability of the new model is shorter, but observationally high-frequency signals are generally only detectable above the noise level at shorter distances. Coefficients n_{ij} ($i = 1, 2, 3$; $j = 1, 2, 3$) from the fitting are listed in Table 1. The inclusion of r_0 and f_0 in the model also guarantees that, even though the values of the coefficients are derived using equation (8) with r in kilometers and f in hertz, they are valid for r and f in any units as long as r_0 and f_0 are converted accordingly.

Figure 7 compares the new geometric-spreading model and a power-law model with synthetic P_n amplitudes. The power-law model has an exponent of -1.3 (Sereno *et al.*, 1988). The difference between the new spreading model and synthetic P_n amplitudes is almost indistinguishable. On the other hand, the power-law model deviates from synthetic P_n amplitudes significantly.

Application to Observed Data

The key value of any mathematical model of the physical world is for the model to be able to provide physically reasonable descriptions of observed data. To test the validity and usefulness of the new P_n geometric-spreading model, we correct a set of observed P_n spectral amplitudes for geometric spreading with the new model and estimate the average medium attenuation. We then compare the results with those published in the literature.

We represent observed P_n amplitudes by equation (5). For the purpose of testing the new P_n geometric-spreading model, we simplify equation (5) by assuming that site response is unity for all stations and source radiation patterns can be ignored. We presume that errors introduced by these simplifications are random and should not affect average-attenuation estimates systematically. With known or estimated source moments, an assumed scaling factor K, and a P_n geometric-spreading model, we can estimate the average-attenuation quality factor at each frequency by least-squares fitting the logarithm of source and geometric-spreading corrected spectral amplitudes as a function of epicentral distance.

The observed P_n amplitudes are measured on vertical-component ground-displacement data recorded by stations in and around China and in southern Europe for events in the same region. The same windowing method as the method we employ to measure the synthetic P_n amplitudes is used. Analyst picks reported in global catalogs (from the International Seismological Centre, the U.S. Geological Survey, the International Data Center of the Preparatory Commission for the Comprehensive Nuclear-Test-Ban Treaty Organization, etc.) are used to center the P_n windows. Randall *et al.* (2006) give a more detailed description of the amplitude dataset. We derive source moments from body-wave magnitudes (m_b) reported in the catalogs using the relationship developed by Geller (1976). We use amplitudes only from events with m_b equal to or smaller than 6 to avoid magnitude saturation. We use a simplified version of the scaling factor K expressed as $K(f) = \{4\pi\rho v^3[1 + (f/f_c)^2]\}^{-1}$ using crustal P-wave velocity and the density of the reference Earth model as v and ρ. The source corner frequency f_c is calculated from the source moment using the relationship $\log M_0 = 17.08 - 3.24 \log f_c$ derived by Xie and Patton (1999) from P_n amplitude data recorded in central Asia. For comparison, we use both the new P_n geometric-spreading model and the power-law model with two different exponents, -1.1 (Walter and Taylor, 2002) and -1.3, in the attenuation estimation. When the new spreading model is used, we limit the epicentral distances of the amplitudes used in the estimation to within the distance range where the model is valid. For power-law model corrections, we use amplitudes between 300 (2.7°) and 1668 km (15°). Attenuation is estimated at 0.75, 1.0, 2.0, 4.0, and 6.0 Hz. Figure 8 plots the 1-Hz P_n amplitudes after source and geometric-spreading corrections. The new spreading model is used in the correction. Although the amplitudes show a large scatter, a linear decay trend due to realistic values of medium attenuation is discernible.

Table 2 lists estimated average quality factors using different geometric-spreading corrections from observed P_n amplitudes. Using the power-law spreading model results in some negative values at low frequencies. At high frequencies, the power-law model yields estimates that range from over 1000 to over 5000. On the other hand, Q estimates using the new spreading model are positive and below 700 at all frequencies. These values can be compared with published P-wave quality factors in the mantle lid, as we discuss in the following paragraphs.

Table 1
Coefficients of the New P_n Geometric-Spreading Model

n_{11}	n_{12}	n_{13}	n_{21}	n_{22}	n_{23}	n_{31}	n_{32}	n_{33}
−0.217	1.79	3.16	−1.94	8.43	18.6	−3.39	9.94	20.7

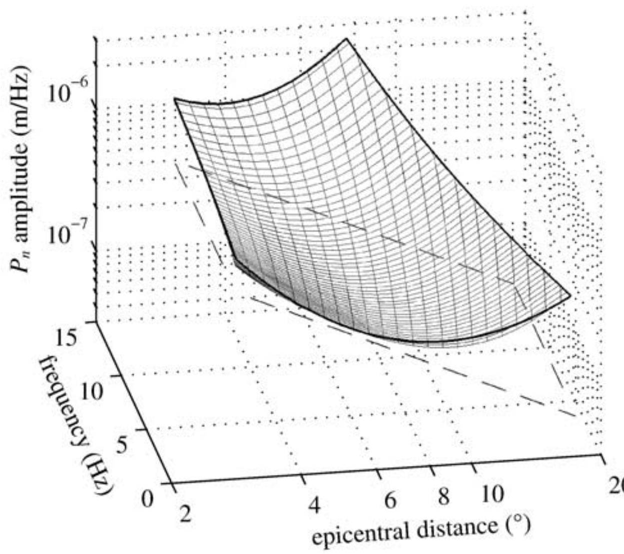

Figure 7. A comparison between synthetic P_n amplitudes, the new P_n geometric-spreading model, and a power-law spreading model with an exponent of -1.3. The meshed surface is synthetic P_n amplitudes. The white, semitransparent surface bounded by the thick line is the new model. The surface outlined by dashed lines is the power-law model.

Using theory, observed body-wave spectra, and waveform modeling, Lundquist and Cormier (1980) derive generic absorption-band *P*-wave *Q* models for the mantle. The *Q* values of these models range from about 100 to 500 for frequencies between 0.7 and 6.0 Hz in the depth range of 45 to 200 km. In their article, Lundquist and Cormier (1980) also cite results of some other *Q* studies that use

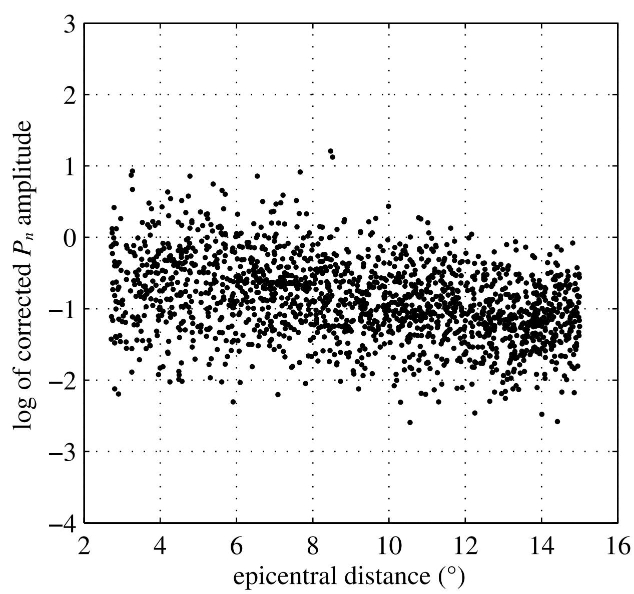

Figure 8. Observed 1-Hz P_n amplitudes corrected for source and geometric spreading. Geometric spreading is corrected for using the new spreading model.

Table 2

Average P_n Quality Factor Estimated Using Different Geometric-Spreading Models

	Data Frequency (Hz)				
	0.75	1.0	2.0	4.0	6.0
New model	440	338	312	557	678
Power-law model 1*	−1669	9241	1206	2204	3450
Power-law model 2†	−734	−2153	1850	3260	5246

*Model with exponent of −1.1.
†Model with exponent of −1.3.

free-oscillation data, long-period surface waves, and high-frequency (1–5 Hz) body waves. The frequency-independent *P*-wave *Q* models from these studies have values from about 100 to 250 for depths between 50 and 150 km. Der *et al.* (1986) construct a *P*-wave *Q* model for the Eurasian Shield using a large set of teleseismic body waves. Their model has values between about 350 and 900 for frequencies between 0.3 and 10 Hz at depths between 100 and 200 km. Above 100 km, *Q* values increase to between 600 and 1500 for the same frequency range.

More recently, some studies make direct P_nQ estimations. Sereno *et al.* (1988) and Sereno (1990) obtain P_nQ models for Scandinavia and eastern Kazakhstan, respectively, by inverting broadband P_n spectra. The 0.75- to 6-Hz P_nQ values that they estimated are between 283 and 768 for Scandinavia and between 260 and 735 for eastern Kazakhstan. Although Sereno *et al.* (1988) and Sereno (1990) assume a power-law P_n geometric-spreading model with an exponent of -1.3, their P_nQ estimates are more in line with the average P_nQ estimates that we obtain using the new P_n spreading model than with those from power-law model corrections (Table 2). A possible explanation for this observation is that the majority of their data are recorded within 1000-km epicentral distance. At short distances, the power-law spreading model has a gentler slope than the new spreading model does (Fig. 7) and therefore would yield smaller *Q* estimates from short-distance data. However, for a broader distance range such as the distance range that our dataset covers, the power-law model yields larger, sometimes negative, *Q* estimates because of the steeper slope of the model at long distances (Fig. 7). The implication is that if a power-law P_n spreading model with a specific exponent is used, it will be applicable only as an approximation in a limited distance range, and models with different exponents are needed for different distance ranges. Our parameterization remedies this failing.

Comparing *Q* values in Table 2 with those published in the literature, we conclude that the new P_n geometric-spreading model yields *Q* estimates that are generally consistent with published results over the broad region of Eurasia. The *Q* estimates with power-law model corrections, on the other hand, have values that are either negative or seem to be too large. It should be noted that *Q* values estimated in this fashion represent only the average P_n attenuation behavior over the broad region of Eurasia. They may not be accurate for any particular region due to the deviation of the uppermost-mantle velocity structure, including velocity gradient and/or heterogeneity, from the constant-velocity structure that we use to develop the geometric-spreading model. The fact that we obtain reasonable Q values from data spanning a large region indicates that the new spreading model at least provides better average behavior than power-law models do and does not result in any peculiarities such as negative Q values.

Variation of Model Parameters Due to Variations of Earth-Model Properties

The new P_n geometric-spreading model is derived by fitting synthetic amplitude data calculated for the reference Earth model. The synthetic P_n amplitudes, and thus the spreading-model parameters, are dependent on the Earth model used in the simulation, as is the case for most general geometric-spreading representations. In order to gauge the dependence of the spreading-model parameters on the variation of 1D Earth-model properties, we conduct additional simulations with different crustal thickness, source depth, and crust/mantle velocity contrast configurations.

We test the effects of crustal thickness on spreading-model parameters by simulating P_n propagation in Earth models with crustal thickness changing from 20 to 70 km, a range of typical of continental crusts (Lay and Wallace, 1995). To test the effects of source depth on the spreading-model parameters, we put the source at depths from 10 to 39 km in a series of simulations. We also vary the crust/mantle velocity contrast to test its effects on the spreading-model parameters. We change the mantle P-wave velocity from 7.6 to 8.6 km/sec with crustal P-wave velocity fixed at 6.5 km/sec. Mantle S-wave velocity and density are adjusted in a similar way. Changing crustal velocities and densities to achieve the same contrast range yields similar results.

Figure 9 shows variations of coefficients n_{ij} relative to reference-model results due to variations of crustal thickness, source depth, and crust/mantle velocity contrast. Most of the large variations of the coefficients are caused by crustal-thickness variation. The effect of the source-depth change is moderate. Crust/mantle velocity contrast has the least effect on the coefficients. Among the coefficients, n_{i1} are the most sensitive, though they are least important in contributing to the spreading model due to their relatively small absolute values (Table 1). Although the coefficients vary considerably due to Earth-model property variations, the overall behavior of the spreading model $G(r, f)$ remains stable. The maximum variation of $G(r, f)$ resulting from coefficient variations shown in Figure 9 is less than 4% for a crustal thickness less than 60 km and less than 10% for a thick crust. Figure 10 plots the variation of Q estimated from observed P_n data due to variation of the coefficients. The plot again shows the relative importance of different Earth model properties in affecting the spreading model. The majority of Q variations are within 10% to 20%. The only large Q variations occur for very thick crust and at long periods.

S_n Simulations

In addition to simulating P_n propagation in a spherical Earth model, we also simulate S_n propagation in the same reference model. Except for different source types and different slowness integration limits, other modeling parameters in the S_n simulation are kept the same as those used in the P_n simulation. Figure 11 plots the $S_n(SH)$ seismograms low-pass filtered below 10 Hz. Compared with Figure 2, the behavior of S_n in a spherical Earth model is very similar to the behavior of P_n waves. The only difference is that the separation of individual waves from the interference wave packet occurs at shorter distances for S_n. This difference can be predicted using equation (4), although the equation was originally derived only for P_n waves. $S_n(SH)$ spectral amplitudes also form a surface with a shape similar to that of the P_n amplitude surface shown in Figure 6.

Because of the similarities between P_n and S_n propagation in a spherical Earth model with constant mantle velocities, we propose an S_n geometric-spreading model that has the same functional form as that of the new P_n spreading model (equations 6 and 7). We derive the values of the coefficients n_{ij} by fitting synthetic $S_n(SH)$ amplitudes. $S_n(SV)$ amplitudes are severely contaminated by P-wave energy up to 1000 km and thus are not suitable for fitting. Beyond 1000 km, $S_n(SV)$ and $S_n(SH)$ amplitudes decay similarly. This suggests that the S_n spreading model developed by fitting $S_n(SH)$ amplitudes is also suitable for describing $S_n(SV)$ geometric spreading.

We correct synthetic $S_n(SH)$ amplitudes for the source moment, the source radiation pattern using takeoff angles calculated with the method described in the Appendix, and the scaling factor K before the fitting. We use $K = (4\pi\rho v^3)^{-1}$, but now v is the S-wave velocity of the crust. We again set the lower-distance limit to 300 km (2.7°) for amplitudes used in the fitting. The upper distance limits are from 6.2° to 14.4° for frequencies from 13 Hz to 0.75 Hz. The limits set the distance range within which the S_n spreading model is valid. Table 3 lists the coefficients n_{ij} for the S_n geometric-spreading model from the fitting.

Discussion

The continental uppermost mantle, where the main portions of the P_n and S_n travel paths are located, is one of the most complex regions in the Earth. The geometric and elastic complexities of the uppermost mantle that affect P_n and S_n geometric spreading include the variation of Moho depth, the mantle-lid velocity gradient, and lateral velocity heterogeneities. Some of these complexities may have comparable or larger effects on P_n and S_n geometric spreading

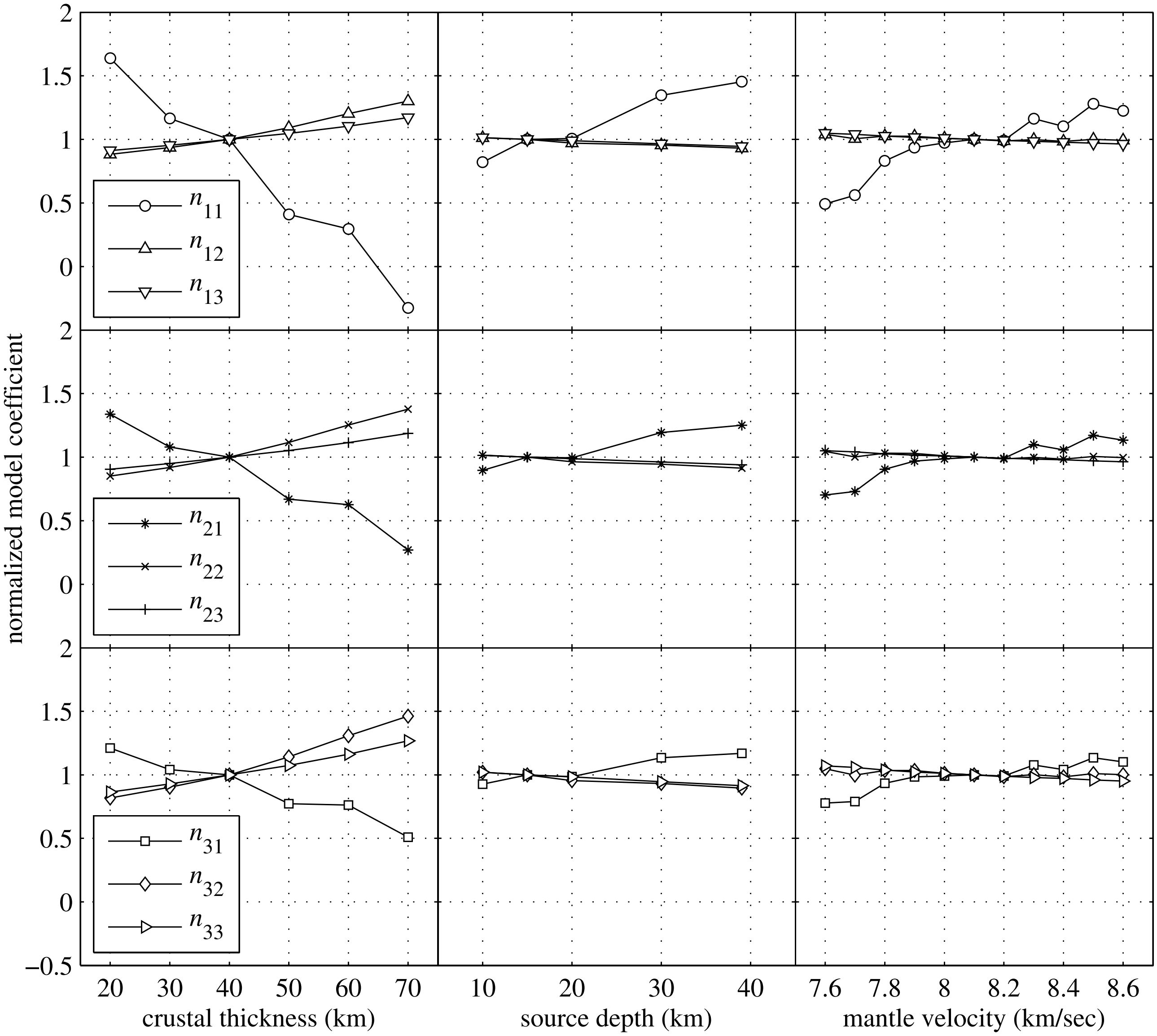

Figure 9. Variations of coefficients n_{ij} of the P_n spreading model due to variations of crustal thickness, source depth, and crust/mantle velocity contrast. Variations are presented as coefficients for different Earth-model properties normalized by reference-model coefficients in Table 1.

than the Earth's sphericity does in some regions of the world. For example, Xie and Patton (1999) attribute the large P_n amplitude variation across a small-aperture seismic array in central Asia to the varying Moho depth in the region. Zhao (1993) obtain a mantle-lid P-wave velocity gradient of 8.0×10^{-4} sec^{-1} for the Basin and Range province in the United States. Using the same method, Zhao and Xie (1993) estimate a P-wave mantle-lid velocity gradient of 3.1×10^{-3} sec^{-1} for the Tibetan Plateau region in China. The average uppermost-mantle P-wave velocity gradient for northern Eurasia that Morozova *et al.* (1999) derive from the Russian Deep Seismic Sounding data is on the order of 4×10^{-3} sec^{-1}. For comparison, the reference-model P-wave velocity gradient resulting from the EFT, which causes the geometric spreading of P_n and S_n to deviate significantly from that of the conical head waves, is 1.3×10^{-3} sec^{-1} at the top of the mantle.

Whereas strong positive mantle-lid velocity gradients constrained from observed data are reported in some regions of the world, there are also studies with different results and conclusions. Hill (1971) infers from seismic data and laboratory measurements that a negative crustal and upper-mantle velocity gradient is likely to exist in high heat-flow regions like the Basin and Range province. Tittgemeyer *et al.* (2000) argue that, from a petrological and petrophysical point of view, a widespread positive velocity gradient in the upper

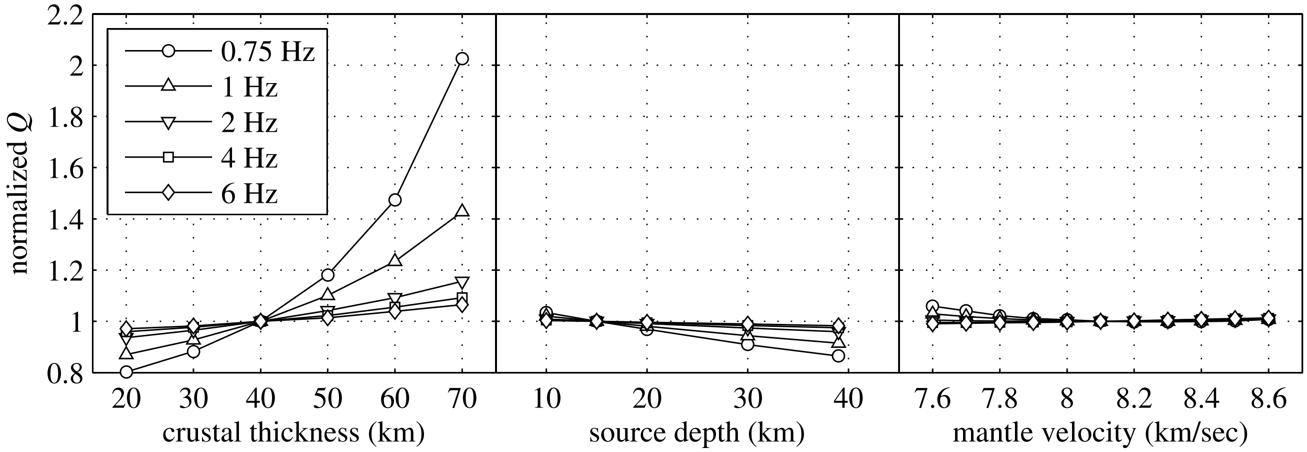

Figure 10. Variations of Q estimated from observed data due to variations of spreading-model coefficients. Variations are presented as Q estimates obtained using different coefficients shown in Figure 9 normalized by Q estimates using coefficients in Table 1.

mantle is not expected and that the observation of teleseismic P_n in the Russian Deep Seismic Sounding data can be explained by the existence of lateral velocity heterogeneity in the uppermost mantle. This model is in contrast with the model advocated by Morozov *et al.* (1998) and Nielsen and Thybo (2003) that the presence of the strong positive upper-mantle velocity gradient and lower-crust velocity heterogeneity is the reason for the observed teleseismic P_n.

Even though unique and reliable determination of the detailed uppermost-mantle velocity structure remains challenging, it is evident that the continental uppermost mantle generally has complexities that affect, sometimes strongly, the P_n and S_n propagation including their geometric spreading. The geometric-spreading models that we propose serve only as first-order approximations that account for the effect of the Earth's sphericity for the simple reference model with constant mantle-lid velocities. Nevertheless, our geometric-spreading models are more appropriate for representing P_n and S_n behavior in the real Earth than the standard power-law model. This conclusion is supported by synthetic simulations and by our successful application of the model on observed P_n data spanning wide distance ranges in Eurasia to yield reasonable attenuation estimates.

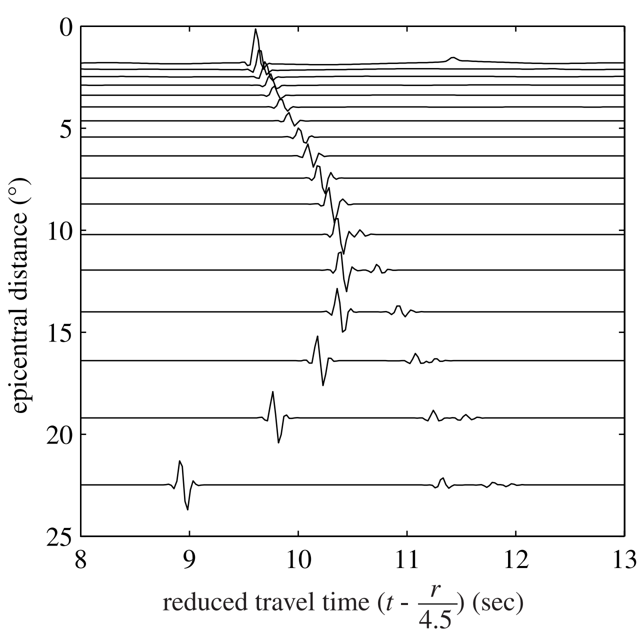

Figure 11. Synthetic $S_n(SH)$ seismograms from calculations using the reference model. The seismograms are filtered below 10 Hz. Travel time is reduced by 4.5 km/sec. r is epicentral distance in kilometers.

The new P_n and S_n geometric-spreading models are useful in common situations where only simple velocity models with uppermost-mantle structure represented as constant-velocity half-space are available. If the mantle-lid velocity gradient is well resolved in a given region, simulations for that gradient can be performed to obtain appropriate geometric-spreading corrections. Because the effect of sphericity is equivalent to the effect of a positive velocity gradient in a plane-layered model, we anticipate that the functional form of our geometric-spreading models will remain the same for Earth models in which an effective (physical plus effects of the sphericity) positive velocity gradient exists. Only the coefficients will differ.

Quantifying the effects of specific mantle-lid velocity gradients, Moho irregularity and lateral velocity heterogeneity in the uppermost mantle on P_n and S_n geometric spreading through 2D and 3D numerical modeling will be the subject of a separate study. It is reasonable to assume that, except for velocity gradients, these effects contribute primarily to scatter around the fundamental behavior of our geometric-spreading models.

Conclusions

We perform detailed numerical modeling to characterize P_n and S_n propagation in a spherical Earth model with con-

Table 3
Coefficients of the New $S_n(SH)$ Geometric-Spreading Model

n_{11}	n_{12}	n_{13}	n_{21}	n_{22}	n_{23}	n_{31}	n_{32}	n_{33}
−0.347	2.16	3.54	−2.69	10.1	20.4	−4.38	11.7	23.1

stant mantle velocities. The results show that P_n and S_n behave in a complex manner in a spherical Earth model, which is consistent with theory predictions. The geometric spreading of P_n and S_n evolves from that of a conical head-wave in a plane-layered Earth model at distances close to the critical distance to that of a direct or diving wave at teleseismic distances. More complexities are introduced by the interference of waves reflected at the underside of Moho and the separation of individual components from the interference wave packet, especially the separation of the direct wave. The complex patterns of P_n and S_n geometric spreading are also frequency dependent with higher frequencies being more affected by the sphericity.

Based on the modeling results, we propose empirical frequency-dependent P_n and S_n geometric-spreading models for a category of spherical Earth models with constant mantle velocities. The new spreading models accurately capture synthetic P_n and S_n amplitude behavior. The P_n spreading model also results in reasonable average-attenuation estimates when applied to observed P_n amplitude data for a broad region of Eurasia.

Variations of Earth-model properties such as crustal thickness, source depth, and crust/mantle velocity contrast within reasonable ranges cause considerable variations of spreading-model parameters. However, the overall behavior of the spreading model is insensitive to variations of these Earth-model properties. Except for long-period waves traveling through very thick crusts, variations of estimated Q from observed data resulting from variations of model parameters are within 20%.

If the velocity structure in the uppermost mantle can be accurately determined for a given region, specific geometric-spreading relations should be predicted by numerical simulations. Otherwise, our new P_n and S_n geometric-spreading models provide reference behavior of P_n and S_n spreading for the common class of spherical Earth models with constant uppermost-mantle velocities. The use of these models should result in a smaller error in different applications compared with using power-law models.

Acknowledgments

We thank George Randall of Los Alamos National Laboratory for his reflectivity code, which played a crucial role in the successful execution of this project, and for his help in debugging the code. George Randall also provided valuable recommendations that resulted in a better parameterization of the new spreading model. Steve Taylor of Rocky Mountain Geophysics was involved in many fruitful discussions during the course of the project. He also suggested a better approach to estimate spreading-model parameters. Vlastislav Červený of Charles University, Czech Republic, patiently answered many questions about the nature of P_n asked by the first author. Diane Baker of Los Alamos National Laboratory was responsible for the collection and measurement of observed P_n amplitude data. Bill Walter and an anonymous reviewer provided helpful reviews of the manuscript. This work was performed under the auspices of the U.S. Department of Energy by Los Alamos National Laboratory and the University of California Santa Cruz under Contract Number DE-AC52-06NA25396 and Contract Number DE-FC52-05NA26606.

References

Aki, K., and P. G. Richards (2002). *Quantitative Seismology*, Second Ed., University Science Books, Sausalito, California.

Bowman, J. R., and B. L. N. Kennett (1991). Propagation of L_g waves in the North Australian Craton: influence of crustal velocity gradients, *Bull. Seismol. Soc. Am.* **81,** 592–610.

Buldyrev, V. S., and A. I. Lanin (1965). Interfering waves at the surface of an elastic inhomogeneous sphere, *Rev. Geophys.* **3,** 49–54.

Červený, V., and R. Ravindra (1971). *Theory of Seismic Head Waves*, University of Toronto Press, Toronto.

Chapman, C. H. (1973). The Earth flattening transformation in body wave theory, *Geophys. J. R. Astr. Soc.* **35,** 55–70.

Chapman, C. H., and J. A. Orcutt (1985). The computation of body wave synthetic seismograms in laterally homogeneous media, *Rev. Geophys.* **23,** 105–163.

Chun, K. Y., R. J. Kokoski, and G. F. West (1989). High-frequency P_n attenuation in the Canadian Shield, *Bull. Seismol. Soc. Am.* **79,** 1039–1053.

Denny, M. D., and L. R. Johnson (1991). The explosion seismic source function: models and scaling laws reviewed, in *Explosion Source Phenomenology*, S. R. Taylor, H. J. Patton and P. G. Richards (Editors), American Geophysical Union, Washington, D.C., 1–24.

Der, Z. A., A. C. Lees, and V. C. Cormier (1986). Frequency dependence of Q in the mantle underlying the shield areas of Eurasia. III. The Q model, *Geophys. J. Int.* **87,** 1103–1112.

Geller, R. J. (1976). Scaling relations for earthquake source parameters and magnitudes, *Bull. Seismol. Soc. Am.* **66,** 1501–1523.

Hartse, H. E., S. R. Taylor, W. S. Phillips, and G. E. Randall (1997). A preliminary study of regional seismic discrimination in central Asia with emphasis on western China, *Bull. Seismol. Soc. Am.* **87,** 551–568.

Hill, D. P. (1971). Velocity gradients and anelasticity from crustal body wave amplitudes, *J. Geophys. Res.* **76,** 3309–3325.

Hill, D. P. (1973). Critically refracted waves in a spherically symmetric radially heterogeneous Earth model, *Geophys. J. R. Astr. Soc.* **34,** 149–177.

Igel, H., and M. Weber (1995). SH-wave propagation in the whole mantle using high-order finite differences, *Geophys. Res. Lett.* **22,** 731–734.

Kennett, B. L. N. (1983). *Seismic Wave Propagation in Stratified Media*, Cambridge University Press, Cambridge, London.

Lay, T., and T. C. Wallace (1995). *Modern Global Seismology*, Academic Press, San Diego, California.

Lundquist, G. M., and V. C. Cormier (1980). Constraints on the absorption band model of Q, *J. Geophys. Res.* **85,** 5244–5256.

Menke, W. H., and P. G. Richards (1980). Crust-mantle whispering gallery phases: a deterministic model of teleseismic $\mathrm{P_n}$ wave propagation, *J. Geophys. Res.* **85,** 5416–5422.

Morozov, I. B., E. A. Morozova, S. B. Smithson, and L. N. Solodilov (1998). On the nature of the teleseismic P_n phase observed on the ultralong-range profile "Quartz," Russia, *Bull. Seismol. Soc. Am.* **88,** 62–73.

Morozova, E. A., I. B. Morozov, and S. B. Smithson (1999). Heterogeneity of the uppermost mantle beneath Russian Eurasia from the ultra-long-range profile QUARTZ, *J. Geophys. Res.* **104,** 20,329–20,348.

Müller, G. (1977). Earth-flattening approximation for body waves derived from geometric ray theory—improvements, corrections and range of applicability, *J. Geophys.* **42,** 429–436.

Nielsen, L., and H. Thybo (2003). The origin of teleseismic *Pn* wave: multiple crustal scattering of upper mantle whispering gallery phases, *J. Geophys. Res.* **108,** no. B10, 2460, doi 10.1029/2003JB002487.

Randall, G. E. (1994). Efficient calculation of complete differential seismograms for laterally homogeneous earth models, *Geophys. J. Int.* **118,** 245–254.

Randall, G. E., X. Yang, H. E. Hartse, M. Maceira, M. D. Arrowsmith, and S. R. Taylor (2006). Regional event identification research in Asia, in *Proc. of the 28th Seismic Research Review: Ground-Based Nuclear Explosion Monitoring Technologies*, 19–21 September 2006, Orlando, Florida, 654–664.

Sereno, T. J. (1990). Frequency-dependent attenuation in eastern Kazakhstan and implications for seismic detection threshold in the Soviet Union, *Bull. Seismol. Soc. Am.* **80,** 2089–2105.

Sereno, T. J., and J. W. Given (1990). P_n attenuation for a spherically symmetric Earth model, *Geophys. Res. Lett.* **17,** 1141–1144.

Sereno, T. J., S. R. Bratt, and T. C. Bache (1988). Simultaneous inversion of regional wave spectra for attenuation and seismic moment in Scandinavia, *J. Geophys. Res.* **93,** 2019–2035.

Street, R. L., R. B. Herrmann, and O. W. Nuttli (1975). Spectral characteristics of the L_g wave generated by central United States earthquakes, *Geophys. J. R. Astr. Soc.* **41,** 51–63.

Taylor, S. R., A. A. Velasco, H. E. Hartse, W. S. Phillips, W. R. Walter, and A. J. Rodgers (2002). Amplitude corrections for regional seismic discriminants, *Pure Appl. Geophys.* **159,** 623–650.

Tinker, M. A., and T. C. Wallace (1997). Regional phase development of the non-proliferation experiment, *Bull. Seismol. Soc. Am.* **87,** 383–395.

Tittgemeyer, M., F. Wenzel, and K. Fuchs (2000). On the nature of P_n, *J. Geophys. Res.* **105,** 16,173–16,180.

Walter, W. R., and S. R. Taylor (2002). UCRL-ID-146882 A revised magnitude and distance amplitude correction (MDAC2) procedure for regional seismic discriminants: theory and testing at NTS, Lawrence Livermore National Laboratory, 13 pp.

Xie, X.-B., and T. Lay (1994). The excitation of Lg waves by explosions: a finite-difference investigation, *Bull. Seismol. Soc. Am.* **84,** 324–342.

Xie, J., and H. J. Patton (1999). Regional phase excitation and propagation in the Lop Nor region of central Asia and implications for P/Lg discriminants, *J. Geophys. Res.* **104,** 941–954.

Yang, X. (2002). A numerical investigation of L_g geometric spreading, *Bull. Seismol. Soc. Am.* **92,** 3067–3079.

Zhao, L. S. (1993). Lateral variations and azimuthal isotropy of P_n velocities beneath Basin and Range province, *J. Geophys. Res.* **98,** 22,109–22,122.

Zhao, L. S., and J. Xie (1993). Lateral variations in compressional velocities beneath the Tibetan Plateau from P_n traveltime tomography, *Geophys. J. Int.* **115,** 1070–1084.

Zhu, T., K. Y. Chun, and G. F. West (1991). Geometrical spreading and Q of P_n waves: an investigative study in eastern Canada, *Bull. Seismol. Soc. Am.* **81,** 882–896.

Appendix A

Incident (Takeoff)-Angle Calculation and Free-Surface Effect Correction

We calculate amplitudes of incoming P_n waves by removing free-surface effects from vertical ground-displacement amplitudes recorded at the Earth's surface. We use the reflection coefficients for plane interfaces (e.g., Lay and Wallace, 1995, Table 3.1) to approximate reflection coefficients for the curved interface. Because we use the corrected amplitudes only for qualitative comparisons (Fig. 5), this approximation is accurate enough.

Different components of the P_n wave packet have different incident angles for a given distance. We use the incident angle of the direct-wave component as an approximation of the incident angle of the whole P_n wave packet at short distances. Because the direct wave is the main component of P_n and the incident angle varies significantly only at long epicentral distances where we measure P_n amplitudes from the direct wave, this approximation is justified. Ignoring the velocity gradient in the single-layer crust resulting from the EFT, equation 6.8 of Červený and Ravindra (1971) states that the incident angle θ of the direct-wave component of P_n is related to epicentral distance r as

$$r = (2H - d)\tan\theta + \frac{2v_m\sqrt{v_c^2 - v_m^2\sin^2\theta}}{gv_m\sin\theta}. \qquad \text{(A1)}$$

The symbols in equation (A1) have the same meanings as those in equation (4) in the main text. For a certain epicentral distance r, we can find the corresponding P_n incident angle at the Earth's free-surface from equation (A1). Tests have shown that taking the velocity gradient in the crust from the EFT, which affects the first term on the right-hand side of equation (A1), into consideration in calculating the incident angle yields essentially the same result.

The takeoff angle of P_n at the source is the same as its incident angle at the free-surface. We assume that equation (A1) can also be used to calculate the S_n takeoff angle.

Geophysics Group
Earth and Environment Sciences Division
Los Alamos National Laboratory
EES-11, MS D408
Los Alamos, New Mexico 87545
(X.Y.)

Department of Earth and Planetary Sciences
University of California, Santa Cruz
Santa Cruz, California 95064
(T.L.)

Institute of Geophysics and Planetary Physics
University of California, Santa Cruz
Santa Cruz, California 95064
(X.-B.X.)

Arctic Region Supercomputing Center
University of Alaska, Fairbanks
Fairbanks, Alaska 99775
(M.S.T.)

Manuscript received 14 February 2007